

Spin Superfluidity in the $\nu = 0$ Quantum Hall State of Graphene

So Takei,^{1,2} Amir Yacoby,³ Bertrand I. Halperin,³ and Yaroslav Tserkovnyak²

¹*Department of Physics, Queens College of the City University of New York, Queens, New York 11367, USA*

²*Department of Physics and Astronomy, University of California, Los Angeles, California 90095, USA*

³*Department of Physics, Harvard University, Cambridge, Massachusetts 02138, USA*

(Received 11 December 2015; revised manuscript received 10 March 2016; published 27 May 2016)

Strong electron interactions can lead to a variety of broken-symmetry phases in monolayer graphene. In the quantum Hall regime, the interaction effect are enhanced by the formation of highly degenerate Landau levels, catalyzing the emergence of such phases. Recent magnetotransport studies show evidence that the $\nu = 0$ quantum Hall state of graphene is in an insulating canted antiferromagnetic phase with the Néel vector lying within the graphene plane. Here, we show that this Néel order can be detected via two-terminal spin transport. We find that a dynamic and inhomogeneous texture of the Néel vector can mediate nearly dissipationless (superfluid) transport of spin angular momentum polarized along the z axis, which could serve as a strong support for the antiferromagnetic scenario. The injection and detection of spin current in the $\nu = 0$ region can be achieved using the two spin-polarized edge channels of the $|\nu| = 2$ quantum Hall state. Measurements of the dependence of the spin current on the length of the $\nu = 0$ region would provide direct evidence for spin superfluidity.

DOI: 10.1103/PhysRevLett.116.216801

Introduction.—The unique electronic properties of graphene (a monolayer of graphitic carbon) stem from its hexagonal crystal structure, giving rise to relativistic effects at electronic velocities well below the speed of light [1]. Graphene is the thinnest and the strongest of 2D materials, and an outstanding electrical and heat conductor, holding great promise as a building block for future electronic devices [2]. A hallmark of graphene’s electronic properties is manifested in magnetotransport. For instance, graphene’s integer quantum Hall (QH) states with anomalous filling fractions $\nu = \pm 4(n + 1/2)$ [3] directly reflect the weakly interacting massless relativistic nature of its low-energy excitations and the fourfold degeneracy associated with the electron spin and valley isospin. The valley degree of freedom distinguishes between the two inequivalent “Dirac points” in the Brillouin zone where the conduction and valence bands of graphene touch [4].

Under high enough magnetic fields, electron-electron interactions can give rise to additional QH states [5,6], including the $\nu = 0$ state at the charge neutrality point. The appearance of the $\nu = 0$ QH state indicates that electron-electron interactions can induce SU(4)-symmetry breaking within the spin-valley space and lift the fourfold degeneracy of the zeroth Landau level [7,8]. A challenge is to understand precisely how this symmetry is broken. Charge-transport experiments, utilizing both the two-terminal and Hall-bar geometries, suggest that the bulk and edge charge excitations for the state are gapped [5]. Furthermore, the recent observation of gapless edge-state reconstruction in a tilted magnetic field [6] is consistent with the scenario where the $\nu = 0$ ground state is a canted antiferromagnetic (CAF) insulator [7]. In the CAF state, the spins S_A on

sublattice A and the spins S_B on sublattice B have different relative orientations; in the presence of an external magnetic field \mathbf{B} normal to the graphene plane (defined to be the xy plane), the total spin $S_A + S_B$ points antiparallel to the field while the Néel vector $S_A - S_B$ lies in the graphene plane. Despite these recent developments, a more direct experimental verification of this CAF scenario would be highly desirable.

Essentially disjoint from the field of graphene QH physics, the field of spintronics is witnessing an increasing interest in realizing spin transport through magnetic insulators via coherent collective magnetic excitations, which allows for superfluid (nearly dissipationless) transport of spin [9,10]. A recent theoretical work has shown that such superfluid spin transport can be realized in antiferromagnetic insulators using a two-terminal device [10]: by laterally attaching two strongly spin-orbit-coupled normal metals at two opposite ends of the insulator, both spin injection and detection could be achieved via electrical means using direct and inverse spin Hall effects. Transplanting this idea to the purported $\nu = 0$ CAF state in graphene, superfluid transport of spin polarized along the z axis could be supported by the CAF via a dynamic Néel texture that rotates about the z axis within the graphene plane [10]. The observation of such spin superfluidity would constitute direct evidence for the CAF scenario. Moreover, graphene is an ideal candidate for the observation of superfluid transport because the spin anisotropy should be extremely small in this system.

Superfluid spin transport.—We begin with a heuristic discussion of how superfluid spin transport through the CAF state can be achieved. We propose a device shown in

Fig. 1(a), where the central CAF region is sandwiched by two $\nu = -2$ QH regions; we ignore the effects of thermal fluctuations of the spins in the CAF. Spin injection into the CAF is achieved using the two copropagating edge channels of the left $\nu = -2$ region. Based on the theory of QH ferromagnetism [11] these edge channels, away from the injection region [shaded in green, which includes the vertices labeled by a and b (represented by red circles in Fig. 1(a)), and the line junction linking the two vertices], are in oppositely polarized spin states (labeled \uparrow, \downarrow)

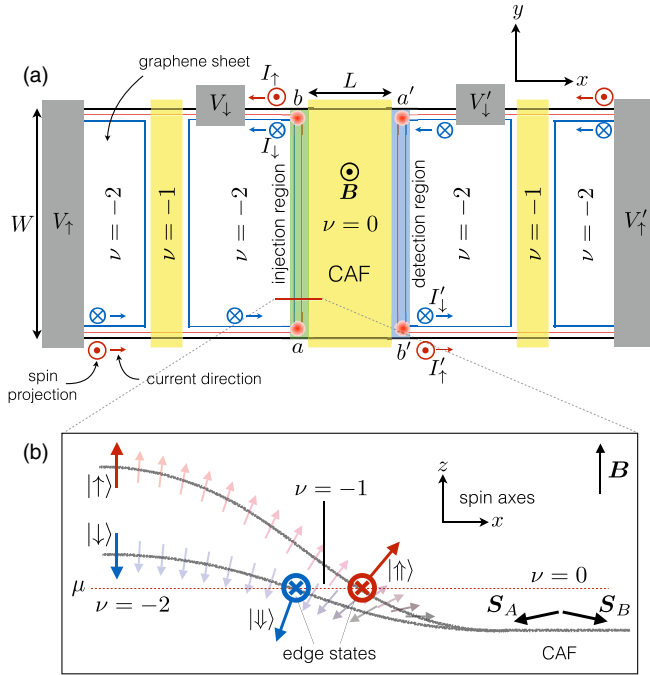


FIG. 1. Proposed setup for realizing and detecting superfluid spin transport through the $\nu = 0$ QH state of graphene. (a) Top view of the graphene Hall bar. The yellow regions are top gates and the gray regions denote Ohmic contacts held at their respective voltages. Two independently biased spin-polarized edge channels on opposite sides of the $\nu = 0$ region are used to inject and detect spin current flowing through the CAF. The spin states of the $\nu = -2$ edge channels are polarized collinearly to the z axis outside of the injection and detection regions. (b) A cartoon energy diagram at a $\nu = 0$ to $\nu = -2$ transition region (across the bold red line). The spin axes are viewed from the side along the y direction. In the $\nu = -2$ region, the energies of the two spin states, oppositely polarized along the z axis, are drawn; the Zeeman effect gives an energetic advantage to the spin-down state. In the $\nu = 0$ region, the two occupied branches of the CAF spectrum are shown. There, an external field in the positive z direction results in a ferromagnetic canting of spins in the negative z direction inside the antiferromagnet. Spin orientations of the chiral edge modes are intermediate between the up and down spin eigenstates within the $\nu = -2$ region (left side) and the canted spins within the CAF (right side). The black lines are merely a rough guide for the energies of the spin states in the transition region. The above illustration does not contain two other branches of the spectrum that are a part of the zeroth Landau level but not essential for the edge physics in the transition region.

collinear with the external field (along the z axis). The two edge channels are expected to undergo very little equilibration outside the injection region [12], so that they can be independently biased by the reservoirs from which they originate, i.e., V_σ .

Figure 1(b) shows a cut across the bold red line in Fig. 1(a) viewed from the side along the y direction. Because of an applied field B normal to the graphene plane and antiferromagnetic correlations induced by electron interactions, spins S_A on sublattice A and S_B on sublattice B in the CAF state lie nearly antiparallel within the graphene plane with a slight canting out of the plane by an angle determined by the ratio between the valley isospin anisotropy and Zeeman energy scales [8]. As shown in Fig. 1(b), the spin quantization axes of the edge states along the line junction may deviate away from the $\pm z$ directions due to the effective field created by the neighboring CAF. We label these canted spin states by \uparrow and \downarrow .

When $V_\uparrow > V_\downarrow$, interchannel scattering may occur inside the injection region, entailing redistributed charge currents I_\uparrow and I_\downarrow emanating from the region and a net loss of spin (polarized along the z axis) inside the region. Neglecting any external sources of spin loss in the injection region (e.g., spin-orbit coupling, magnetic impurities, etc.), the net spin lost in the edge should be absorbed by the CAF, leading to the injection of spin current (hereafter always defined to be the component polarized along the z axis) into the CAF. This will induce the CAF into a dynamic steady state, in which the local Néel vector in the CAF rotates about the z axis with a global frequency Ω (see Fig. 2) [10]. The dynamic Néel texture will, in turn, pump spin current [13] out into the edge channels in the detection region, resulting in the transport of spin from the injection to the detection side [the detection region, involving vertices a' and b' , is shaded in blue in Fig. 1(a)]. We initially leave the two detection channels unbiased, i.e., $V'_\uparrow = V'_\downarrow$ such that the spin current entering the detection region is zero. However, the injection of spin current from the CAF into

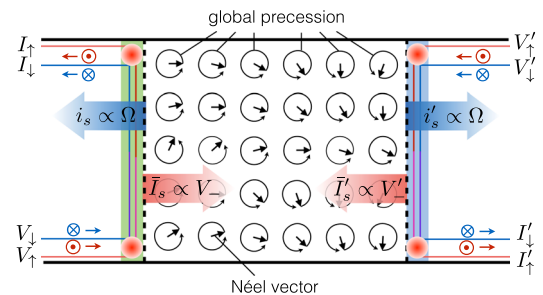


FIG. 2. A cartoon of the CAF in a dynamic superfluid state. The Néel vector rotates within the graphene plane about the z axis with a global precession frequency Ω . The static contribution to spin current $\bar{I}_s \propto V_- = V_\uparrow - V_\downarrow$ is injected into the CAF while the dynamic (spin-pumping) contribution $i_s \propto \Omega$ pumps spin current back out into the edge. Two analogous contributions exist on the detection side.

the detection edge will generate a redistribution of charges on the two channels, and result in $I'_\uparrow \neq I'_\downarrow$. Therefore, the spin current ejected at the detection edge is directly determined by measuring the spin current exiting the detection region.

Phenomenology and main results.—We now place the above heuristic discussion on more quantitative grounds. The discussion below closely follows Ref. [10]. Once the dynamic steady state is established in the CAF, the spin current I_s entering the CAF at the injection edge has two contributions: $I_s = \bar{I}_s + i_s$, where \bar{I}_s is the spin current injected into a static CAF in equilibrium, and i_s is the spin-pumping (dynamic) contribution describing spin current pumped back out to the edge due to the nonequilibrium Néel dynamics (see Fig. 2) [13]. The static contribution, within linear response, reads $\bar{I}_s = (\hbar/2e)[g_Q(V_\uparrow - V_\downarrow) - (\bar{I}_\uparrow - \bar{I}_\downarrow)]$, where $g_Q \equiv e^2/h$ and $e > 0$ is the magnitude of the electron charge; \bar{I}_σ denotes the charge currents emanating from the injection region in the static limit. Because of charge conservation, and the fact that equally biased edge channels lead to equal outgoing charge currents (i.e., $V_\uparrow = V_\downarrow$ implying $\bar{I}_\uparrow = \bar{I}_\downarrow$), the charge currents emanating from the injection region can be written generally as $\bar{I}_\sigma = g_Q[V_+ + \sigma(1 - \gamma)V_-]/2$, where $V_\pm = V_\uparrow \pm V_\downarrow$ and $\sigma = \pm$ corresponds to the \uparrow and \downarrow channels, respectively. The real parameter $0 \leq \gamma \leq 1$ characterizes the strength of interchannel scattering in the injection region (it is explicitly computed using a simple microscopic model later in this work). The limit of no interchannel scattering corresponds to $\gamma = 0$, while the limit of strong scattering (full equilibration between the channels) corresponds to $\gamma = 1$. Inserting \bar{I}_σ into the expression for \bar{I}_s , one obtains

$$\bar{I}_s = \frac{\hbar}{2e} g_Q \gamma V_- . \quad (1)$$

The dynamical contribution i_s follows from Eq. (1) via Onsager reciprocity. To see this, we first define two continuum variables in the CAF that are slowly varying on the scale of the magnetic length: $\mathbf{n}(\mathbf{x})$ and $\mathbf{m}(\mathbf{x})$, $\mathbf{n}(\mathbf{x})$ being the unit vector pointing along the local Néel order and $\mathbf{m}(\mathbf{x})$ being the local spin density. The uniform frequency Ω of the rotating Néel texture effectively acts as an additional magnetic field in the z direction, introducing a uniform canting of the CAF spins along the z direction in addition to the existing canting due to the external field. Therefore, the dynamic steady state is characterized by a uniform $\mathbf{m}(\mathbf{x}) = m_z \mathbf{e}_z$. Defining the total spin $M_z = m_z L W$, where L and W are the dimensions of the CAF region [see Fig. 1(a)], the temporal change in M_z , in the presence of the injected spin current I_s , should read

$$\dot{M}_z = I_s + \dots , \quad (2)$$

where the ellipsis denotes terms arising from the intrinsic dynamics within the CAF. Inserting the static contribution (1) for I_s in Eq. (2) introduces terms linear in V_\uparrow and V_\downarrow , which are the forces conjugate to the charge currents I_\uparrow and I_\downarrow , respectively. Onsager reciprocity then endows the static contributions \bar{I}_σ with a dynamic contribution as

$$I_\sigma = \bar{I}_\sigma - \sigma \frac{\hbar}{2e} g_Q \gamma f_{M_z} , \quad (3)$$

where $f_{M_z} \equiv -\delta_{M_z} F$ is the force conjugate to M_z and F is the free energy of the CAF [in obtaining Eq. (3), we have assumed a symmetry \mathcal{S} of the device in Fig. 1(a) under time reversal followed by a π spatial rotation about the x axis]. Noting that the force f_{M_z} relates to the local Néel vector via $f_{M_z} = -(\mathbf{n} \times \dot{\mathbf{n}}) \cdot \mathbf{e}_z \approx -\Omega$ [10], the total injected spin current $I_s = (\hbar/2e)[g_Q(V_\uparrow - V_\downarrow) - (I_\uparrow - I_\downarrow)]$ can be obtained using Eq. (3) as $I_s = (\gamma/4\pi)(eV_- - \hbar\Omega) \equiv \bar{I}_s + i_s$. Based on an analogous consideration on the detection side, the total spin current injected into the edge from the CAF becomes $I'_s = -(\gamma'/4\pi)(eV'_- - \hbar\Omega) \equiv \bar{I}'_s + i'_s$, where γ' is the interchannel scattering parameter, analogous to γ , for the detection side. Fixing the voltages of the electron reservoirs on the detection side to zero, i.e., $V'_{\uparrow,\downarrow} = 0$, we obtain $I'_s = i'_s$.

In the absence of any sources of spin loss in the CAF bulk (i.e., no Gilbert damping) we have $I_s = I'_s$, and the global frequency should read

$$\hbar\Omega = \frac{\gamma}{\gamma + \gamma'} eV_- . \quad (4)$$

Then, the amount of spin current generated on the detection side by the superfluid spin transport reads

$$I'_s = \frac{1}{4\pi} \frac{\gamma\gamma'}{\gamma + \gamma'} eV_- . \quad (5)$$

Equations (4) and (5) constitute the main results of this work, and they predict that the spin current should be independent of the length L . In graphene, intrinsic spin-orbit effects are very weak, so it should be reasonable to ignore Gilbert damping as a first approximation, as we do here. We discuss the effects of finite Gilbert damping in the Supplemental Material [14]. There, we show that for fixed W and γ, γ' , Gilbert damping leads to a decay in the spin current through the $\nu = 0$ region with the length L .

Since the CAF region has vanishing electrical conductivity the currents I'_\uparrow and I'_\downarrow , which enter the contacts labeled V'_\uparrow and V'_\downarrow , must satisfy $I'_\uparrow + I'_\downarrow = 0$. Therefore, the currents, which may be measured directly, will be related to the transmitted spin current by $I'_\uparrow = -I'_\downarrow = eI'_s/\hbar$.

Kinetic theory for injection and detection regions.—We now develop a simple microscopic model for the

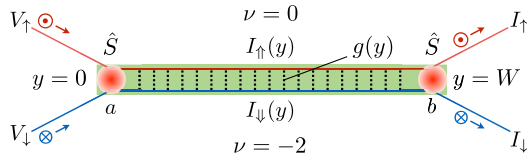


FIG. 3. The injection region. Charge currents entering vertices a and b redistribute according to the scattering probability matrix \hat{S} . The interchannel scattering inside the line junction is quantified by an effective conductance $g(y)$ per unit length.

parameters γ and γ' . On the injection side, γ quantifies the extent to which the two edge channels equilibrate inside the injection region. Within linear response, γ can be evaluated for the (static) CAF in equilibrium. At vertices a and b , the relative spin misalignment between the (\uparrow, \downarrow) and (\uparrow, \downarrow) states together with sources of momentum nonconservation there (e.g., edge disorder and the sharp directional change of the edge) can give rise to interchannel charge scattering. The redistribution of charges at these vertices must obey charge conservation, and can be parametrized by an energy-independent transmission probability $t \in [0, 1]$ (under the assumed symmetry \mathcal{S} , the two vertices are characterized by an identical probability)

$$\begin{pmatrix} I_{\uparrow}(0) \\ I_{\downarrow}(0) \end{pmatrix} = g_Q \hat{S} \begin{pmatrix} V_{\uparrow} \\ V_{\downarrow} \end{pmatrix}, \quad \begin{pmatrix} I_{\uparrow} \\ I_{\downarrow} \end{pmatrix} = \hat{S} \begin{pmatrix} I_{\uparrow}(W) \\ I_{\downarrow}(W) \end{pmatrix}, \quad (6)$$

where $I_{\sigma}(y)$ (with $\sigma = \uparrow, \downarrow$) is the local charge current flowing along the line junction in edge channel σ , $\hat{S} = t\hat{\sigma}_0 + (1-t)\hat{\sigma}_x$ is the scattering probability matrix at the vertices, and $\hat{\sigma}_0$ and $\hat{\sigma}_x$ are the 2×2 identity matrix and the x component of the Pauli matrices, respectively (see Fig. 3).

The occurrence of interchannel scattering within the line junction requires (i) spatial proximity of the two channels, such that there is sufficient overlap of their orbital wave functions, (ii) elastic impurities, providing the momentum nonconserving mechanism necessary to overcome the mismatch in Fermi momenta of the two channels, and (iii) a spin-flip mechanism, assumed here to be provided by the neighboring CAF. All three factors go into defining the interchannel tunneling conductance $g(y)$ per unit length, which we treat phenomenologically here. In terms of $g(y)$, the change in current on channel σ is given by $\delta I_{\uparrow, \downarrow}(y) = \mp g(y)[V_{\uparrow}(y) - V_{\downarrow}(y)]\delta y$, where V_{σ} is the local voltage on edge channel σ [we assume that the edges are always locally equilibrated at all points y such that the voltage at each point is related to the local current through $V_{\sigma}(y) = I_{\sigma}(y)/g_Q$]. Then, the currents inside the line junction satisfy

$$\frac{\partial I_{\uparrow}}{\partial y} = -\frac{\partial I_{\downarrow}}{\partial y} = -\frac{g(y)}{g_Q}[I_{\uparrow}(y) - I_{\downarrow}(y)]. \quad (7)$$

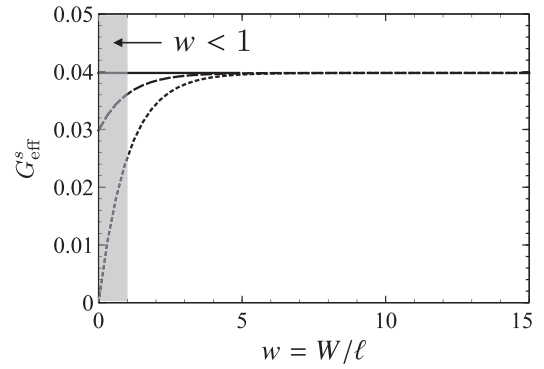


FIG. 4. Effective spin conductance $G_{\text{eff}}^s \equiv I'_s/eV_-$ as a function of the aspect ratio $w = W/\ell$. The solid, dashed, and dotted curves are, respectively, for full ($t = 0.5$), partial ($t = 0.75$), and no ($t = 1$) interchannel mixing at the vertices.

Assuming a position-independent tunneling conductance g and defining the edge equilibration length $\ell \equiv g_Q/2g$, the currents entering vertex b are then given by (see Fig. 3)

$$\begin{pmatrix} I_{\uparrow}(W) \\ I_{\downarrow}(W) \end{pmatrix} = \frac{1}{2} \begin{pmatrix} 1 + e^{-w} & 1 - e^{-w} \\ 1 - e^{-w} & 1 + e^{-w} \end{pmatrix} \begin{pmatrix} I_{\uparrow}(0) \\ I_{\downarrow}(0) \end{pmatrix}, \quad (8)$$

where $w = W/\ell$. Combining Eqs. (6) and (8), we obtain $\gamma = 1 - (1 - 2t)^2 e^{-w}$. A fully analogous consideration on the detection side leads to $\gamma' = 1 - (1 - 2t')^2 e^{-w'}$, where $w' = W/\ell'$, t' is the transmission probability at vertices a' and b' , and ℓ' is the edge equilibration length associated with the line junction on the detection side.

The results are now discussed for the symmetric case, in which $t = t'$ and $\ell = \ell'$. In Fig. 4, we plot the effective spin conductance through the CAF, $G_{\text{eff}}^s \equiv I'_s/eV_-$ [see Eq. (5)], as a function of w for different t . Full mixing of the edge channels at the vertices, i.e., $t = 0.5$, entails local spin injection at vertex a . Therefore, increasing the width of the sample has no effect on the effective spin conductance. If no scattering occurs at the vertices, i.e., $t = 1$, spin current is injected only along the line junction. For widths smaller than the equilibration length, i.e., $w < 1$, increasing the width gives an enhancement in the injected spin current, and a linear increase in $G_{\text{eff}}^s \propto w$ is obtained (see the dotted line). However, as the width increases beyond the equilibration length, spin injection no longer increases and the conductance saturates at a value $1/8\pi$. For partial interchannel mixing at the vertices, $0.5 < t < 1$, some spin current is injected at vertex a so a finite conductance entails even in the limit of $w \rightarrow 0$ (see the dashed line). With increasing width, the conductance also increases until the width, again, reaches of order the edge equilibration length.

Conclusions.—In this work, we present a proposal to detect spin superfluidity in the $\nu = 0$ quantum Hall state of graphene. An observation of long-ranged (superfluid) spin transport through the $\nu = 0$ state will constitute direct evidence for the CAF ground state purported recently.

Important open questions with regard to the feasibility of our proposal relate to the fact that we have only been able to estimate the efficiency of spin transfer between the edges and the CAF state. In particular, we do not have a precise understanding of how the interchannel scattering strength $g(y)$ depends on disorder along the edge and on the profile of the electrostatic potential between the $\nu = 0$ and $\nu = -2$ regions. Furthermore, we do not have a complete knowledge of the possible sources of spin loss in the injection and detection regions. This calls for further detailed theories of the injection and detection mechanisms as well as for experiments testing our proposal in practice.

We would like to thank Dmitry Abanin and Jelena Klinovaja for helpful discussions. This work was supported by FAME (an SRC STARnet center sponsored by MARCO and DARPA). B. I. H. and A. Y. were supported in part by the STC Center for Integrated Quantum Materials under NSF Grant No. DMR-1231319.

-
- [1] A. H. Castro Neto, F. Guinea, N. M. R. Peres, K. S. Novoselov, and A. K. Geim, *Rev. Mod. Phys.* **81**, 109 (2009); S. Das Sarma, S. Adam, E. H. Hwang, and E. Rossi, *ibid.* **83**, 407 (2011).
- [2] F. Schwierz, *Nat. Nanotechnol.* **5**, 487 (2010); **9**, 725 (2014).
- [3] K. S. Novoselov, A. K. Geim, S. V. Morozov, D. Jiang, M. I. Katsnelson, I. V. Grigorieva, S. V. Dubonos, and A. A. Firsov, *Nature (London)* **438**, 197 (2005); Y. Zhang, Y.-W. Tan, H. L. Stormer, and P. Kim, *ibid.* **438**, 201 (2005).
- [4] Y. Zheng and T. Ando, *Phys. Rev. B* **65**, 245420 (2002); V. P. Gusynin and S. G. Sharapov, *Phys. Rev. Lett.* **95**, 146801 (2005); N. M. R. Peres, F. Guinea, and A. H. Castro Neto, *Phys. Rev. B* **73**, 125411 (2006).
- [5] Y. Zhang, Z. Jiang, J. P. Small, M. S. Purewal, Y.-W. Tan, M. Fazlollahi, J. D. Chudow, J. A. Jaszczak, H. L. Stormer, and P. Kim, *Phys. Rev. Lett.* **96**, 136806 (2006); J. G. Checkelsky, L. Li, and N. P. Ong, *ibid.* **100**, 206801 (2008); X. Du, I. Skachko, F. Duerr, A. Luican, and E. Y. Andrei, *Nature (London)* **462**, 192 (2009); K. I. Bolotin, F. Ghahari, M. D. Shulman, H. L. Stormer, and P. Kim, *ibid.* **462**, 196 (2009); L. Zhang, J. Camacho, H. Cao, Y. P. Chen, M. Khodas, D. E. Kharzeev, A. M. Tsvelik, T. Valla, and I. A. Zaliznyak, *Phys. Rev. B* **80**, 241412 (2009); C. R. Dean, A. F. Young, P. Cadden-Zimansky, L. Wang, H. Ren, K. Watanabe, T. Taniguchi, P. Kim, J. Hone, and K. L. Shepard, *Nat. Phys.* **7**, 693 (2011); F. Ghahari, Y. Zhao, P. Cadden-Zimansky, K. Bolotin, and P. Kim, *Phys. Rev. Lett.* **106**, 046801 (2011); A. F. Young, C. R. Dean, L. Wang, H. Ren, P. Cadden-Zimansky, K. Watanabe, T. Taniguchi, J. Hone, K. L. Shepard, and P. Kim, *Nat. Phys.* **8**, 550 (2012).
- [6] A. F. Young, J. D. Sanchez-Yamagishi, B. Hunt, S. H. Choi, K. Watanabe, T. Taniguchi, R. C. Ashoori, and P. Jarillo-Herrero, *Nature (London)* **505**, 528 (2014).
- [7] K. Yang, S. Das Sarma, and A. H. MacDonald, *Phys. Rev. B* **74**, 075423 (2006); M. O. Goerbig, R. Moessner, and B. Doucot, *ibid.* **74**, 161407 (2006); V. P. Gusynin, V. A. Miransky, S. G. Sharapov, and I. A. Shovkovy, *ibid.* **74**, 195429 (2006); K. Nomura and A. H. MacDonald, *Phys. Rev. Lett.* **96**, 256602 (2006); J. Alicea and M. P. A. Fisher, *Phys. Rev. B* **74**, 075422 (2006); D. A. Abanin, P. A. Lee, and L. S. Levitov, *Phys. Rev. Lett.* **96**, 176803 (2006); J.-N. Fuchs and P. Lederer, *ibid.* **98**, 016803 (2007); L. Sheng, D. N. Sheng, F. D. M. Haldane, and L. Balents, *ibid.* **99**, 196802 (2007); D. A. Abanin, K. S. Novoselov, U. Zeitler, P. A. Lee, A. K. Geim, and L. S. Levitov, *ibid.* **98**, 196806 (2007); J. Jung and A. H. MacDonald, *Phys. Rev. B* **80**, 235417 (2009); K. Nomura, S. Ryu, and D.-H. Lee, *Phys. Rev. Lett.* **103**, 216801 (2009); C.-Y. Hou, C. Chamon, and C. Mudry, *Phys. Rev. B* **81**, 075427 (2010); D. A. Abanin, B. E. Feldman, A. Yacoby, and B. I. Halperin, *ibid.* **88**, 115407 (2013); I. F. Herbut, *ibid.* **75**, 165411 (2007); M. Kharitonov, *ibid.* **85**, 155439 (2012); B. Roy, M. P. Kennett, and S. Das Sarma, *ibid.* **90**, 201409 (2014).
- [8] M. Kharitonov, *Phys. Rev. B* **86**, 075450 (2012).
- [9] J. König, M. C. Bönsager, and A. H. MacDonald, *Phys. Rev. Lett.* **87**, 187202 (2001); E. B. Sonin, *Adv. Phys.* **59**, 181 (2010); S. Takei and Y. Tserkovnyak, *Phys. Rev. Lett.* **112**, 227201 (2014); W. Chen and M. Sgrist, *Phys. Rev. B* **89**, 024511 (2014).
- [10] S. Takei, B. I. Halperin, A. Yacoby, and Y. Tserkovnyak, *Phys. Rev. B* **90**, 094408 (2014).
- [11] M. O. Goerbig, *Rev. Mod. Phys.* **83**, 1193 (2011); Y. Barlas, K. Yang, and A. H. MacDonald, *Nanotechnology* **23**, 052001 (2012).
- [12] F. Amet, J. R. Williams, K. Watanabe, T. Taniguchi, and D. Goldhaber-Gordon, *Phys. Rev. Lett.* **112**, 196601 (2014).
- [13] Y. Tserkovnyak, A. Brataas, and G. E. W. Bauer, *Phys. Rev. Lett.* **88**, 117601 (2002); Y. Tserkovnyak, A. Brataas, G. E. W. Bauer, and B. I. Halperin, *Rev. Mod. Phys.* **77**, 1375 (2005).
- [14] See Supplemental Material <http://link.aps.org/supplemental/10.1103/PhysRevLett.116.216801> for a discussion on the effects of Gilbert damping in the canted antiferromagnet region on spin transport.